Journal of The Electrochemical Society, **160** (10) A1653-A1660 (2013)
0013-4651/2013/160(10)/A1653/8/$31.00 © The Electrochemical Society

Supercapacitor Electrodes Produced through Evaporative Consolidation of Graphene Oxide-Water-Ionic Liquid Gels

Michael A. Pope,[a] Sibel Korkut,[a,b] Christian Punckt,[a,b] and Ilhan A. Aksay[a,z]

[a]*Department of Chemical and Biological Engineering, Princeton University, Princeton, New Jersey 08544, USA*
[b]*Vorbeck Princeton Research Center, Vorbeck Materials Corporation, Monmouth Junction, New Jersey 08520, USA*

We use colloidal gels of graphene oxide in a water-ethanol-ionic liquid solution to assemble graphene-ionic liquid laminated structures for use as electrodes in electrochemical double layer capacitors. Our process involves evaporation of water and ethanol yielding a graphene oxide/ionic liquid composite, followed by thermal reduction of the graphene oxide to electrically conducting functionalized graphene. This yields an electrode in which the ionic liquid serves not only as the working electrolyte but also as a spacer to separate the graphene sheets and to increase their electrolyte-accessible surface area. Using this approach, we achieve an outstanding energy density of 17.5 Wh/kg at a gravimetric capacitance of 156 F/g and 3 V operating voltage, due to a high effective density of the active electrode material of 0.46 g/cm^2. By increasing the ionic liquid content and the degree of thermal reduction, we obtain electrodes that retain >90% of their capacitance at a scan rate of 500 mV/s, illustrating that we can tailor the electrodes toward higher power density if energy density is not the primary goal. The elimination of the electrolyte infiltration step from manufacturing makes this bottom-up assembly approach scalable and well-suited for combinations of potentially any graphene material with ionic liquid electrolytes.
© 2013 The Electrochemical Society. [DOI: 10.1149/2.017310jes] All rights reserved.

Manuscript submitted May 21, 2013; revised manuscript received July 4, 2013. Published July 30, 2013.

Electrochemical double layer capacitors (EDLCs), also known as ultracapacitors or supercapacitors, operate by accumulating charge within the electrochemical double layer at the electrode/electrolyte interface.[1] A typical EDLC consists of two electrodes which are imbibed with electrolyte, separated by a porous, ion-permeable membrane, sandwiched between two typically metallic current collectors, and packaged in a hermetically sealed pouch or container. The energy density E of such a device – specific to the entire device mass – is the performance metric of practical interest[1] (alternatively, volume-specific values[2] can be reported). E depends on the gravimetric capacitance C_G of the dry (active) electrode material, the operating voltage U, and the mass fraction f of the active electrode material (typically ~30 wt% for commercially viable devices)[2,3] accounting for the mass of electrolyte, separator, current collectors and packaging:[1,4]

$$E = {}^{f}/_{8} C_G U^2. \quad [1]$$

In order to increase E, research is targeted toward increasing both C_G and U, but the impact of the mass fraction f is often neglected or not reported.[2,5–8] Instead, the energy density is defined as $E^* = 1/8\ C_G U^2$ (often, and incorrectly $E^* = 1/2\ C_G\ U^2$ is used but this does not account properly for the 2-electrode configuration), which excludes the weight contribution of device components other than the active electrode material. The relation between C_G, U, and E^* is illustrated in Figure 1, where we plot E^* vs. C_G for material/electrolyte combinations that can operate at voltages U between 1 and 4 V: High values of C_G up to 1000 F/g can be achieved with materials such as RuO_2,[1] MnO_2,[9] or carbonaceous materials[4,8,10–21] in water-based systems, since these materials are redox active in aqueous electrolytes, i.e., exhibit faradaic reactions akin to processes within batteries (pseudocapacitance). In spite of these high C_G values, however, E^* remains low since aqueous systems are not stable at $U > \sim 2$ V.[22] On the other hand, in order to achieve $E^* = 100$ Wh/kg, an electrode material with $C_G = 200$ F/g suffices if the device can be operated at 4 V. High operating voltages have been attained with organic electrolytes[1] and, more recently, with ionic liquids (ILs)[23,24] which therefore are the electrolyte of choice for high energy density applications. ILs have been used in conjunction with carbonaceous electrodes such as activated carbons, carbide derived carbons (CDCs), or carbon aerogels, achieving stable operation and reaching up to $E^* = 50$ Wh/kg at values of C_G between 100 and 200 F/g.[3,5,7,8,12–14,20,25–29] Besides exploring electrolytes which are stable at voltages in excess of 4 V, maximizing C_G of the carbonaceous electrodes is thus the route toward EDLCs with larger E.

C_G is proportional to the surface area-specific double layer capacitance (C_{DL}) of the electrode material, its mass specific surface area (SSA), and the fraction to which the SSA is accessible to the electrolyte in the final electrode. Due to their exceptionally high theoretical SSA (2630 m^2/g), functionalized graphene sheets (FGSs), derived by the thermal reduction and exfoliation of graphite oxide (GO)[30,31] or the chemical reduction of graphene oxide,[32] are promising candidates for high-performance electrode materials. In addition to high SSA, our recent work suggests that, due to the presence of a large number of lattice defects and functional groups,[30,31,33] the C_{DL} of the FGS/electrolyte interface (14–26 μF/cm^2 in 0.5 M NaF)[34] is not limited by a low electronic density of states as in pristine graphene[35,36] or carbon nanotubes (CNTs)[37] (3–4 μF/cm^2). At the same time, FGSs provide electrical resistivities as low as 8 kΩ/sq.[38,39] Combining FGSs and ILs therefore has the potential to yield materials with C_G reaching 400 F/g (assuming $C_{DL} \approx 20$ μF/cm^2 in IL electrolyte[40] and an ion-accessible SSA of 2000 m^2/g).

However, obtaining a high ion-accessible surface area with FGS electrodes has proven difficult in practice due to aggregation and restacking of sheets during processing.[41] A number of recent studies therefore focused on processing and assembling FGSs into EDLC electrodes in ways such that the ion-accessible surface area was maximized,[3,6–8] yielding C_G and E^* as high as 276 F/g and 150 Wh/kg, respectively (see Figure 1 and Table I). These examples either involve the use of spacers that act as inactive mass ("dead-weight")[7] or involve the imbibition of excessive amounts of electrolyte.[3,6,8] As a result, the effective density of the active graphene material ρ_{eff} in the electrodes is low (see Table I); electrode mass is dominated by the mass of the imbibed electrolyte and, if present, the spacers. The value of ρ_{eff} determines the upper limit for the mass fraction f that can be achieved if the electrode material is used in a device: For a thick electrode, i.e., neglecting the mass of charge collectors, membrane and packaging, f (in wt%) can be approximated as:

$$f \approx \frac{100\rho_{eff} \cdot \rho_a}{\rho_i \cdot (\rho_a - \rho_{eff}) + \rho_{eff} \cdot \rho_a}, \quad [2]$$

where ρ_a and ρ_i denote the densities of the active electrode material and the combined effective density of the inactive components including the electrolyte, respectively. Equation 2 was derived assuming no gas filled voids are present in the material. Values for f derived from published data on FGS-based electrodes (Table I) range from 4 to 25 wt%. Values of E for these FGS-based electrodes (also reported in Table I) are in most cases smaller than those obtained, for example, with CDC electrodes which, due to their denser packing, achieve high values of E despite comparably low C_G.[42] To demonstrate this point, in Figure 1b we show that the energy density drops substantially when f is considered. Electrodes with the highest C_G achieve the lowest E due to excessive amounts of electrolyte used. Therefore, while FGSs exhibit superior gravimetric capacitance, the inability to pack them densely

[z]E-mail: iaksay@princeton.edu

Downloaded on 2013-07-31 to IP 128.112.70.3 address. Redistribution subject to ECS license or copyright; see ecsdl.org/site/terms_use

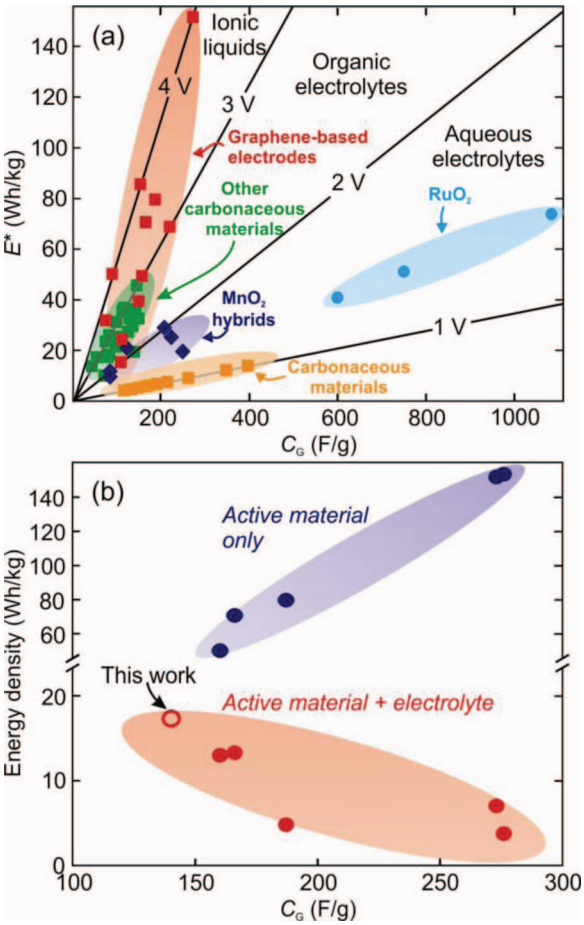

Figure 1. Estimated energy density of a two electrode cell as a function of U and C_G. (a) E^* does not consider device components other than the active material. (b) Comparison of uncorrected (E^*) and corrected (E) energy densities for examples in non-aqueous electrolytes where f could be estimated (see Table I). The literature values do not represent the energy density of a full cell but rather the energy per mass of electrode and electrolyte. This represents the upper limit achievable if electrode capacitance could be maintained for thick electrodes. Recent literature data for graphene-based electrodes in non-aqueous and aqueous electrolytes are shown as red and orange squares, respectively. Data plotted for other materials were taken from several recent reviews. References are given in the main text.

Table I. Comparison of various electrode properties from recent studies demonstrating the highest values of C_G. Energy density was estimated using $E = f/8\ C_G \cdot U^2$.

Approach	C_G (F/g)	ρ_{eff} (g/cm^3)[a]	f (wt%)[a]	E (Wh/kg)
Laser-scribed FGSs[6]	276	0.05	4	5
Hydrated FGSs[8]	273	0.09	7	8
Activation of FGSs[3]	166	0.36	25	13.8
FGSs separated by poly-ILs[7]	164	< 0.12	< 9	< 6
Carbide-derived carbon[25]	160	0.53	35	13.5

[a]Equation 2 was used to estimate either ρ_{eff} or f based on details reported in the cited works: Thermal gravimetric analysis data presented in ref. 7 indicate $f < 9$ wt%; In ref. 8, the water concentration in their films prior to solvent exchange with IL was 92 wt%, which corresponds to ~93 wt% IL if we assume all water is replaced by the IL during solvent exchange and the electrode volume remained constant leading to f ~7 wt%; Ref. 6 reported the mass of active material and electrode dimensions which were used to estimate ρ_{eff}; The volumetric capacitance (C_V) and C_G were reported in ref. 3 and 25 and ρ_{eff} was determined using $\rho_{eff} = C_V/C_G$.

while preserving high ion-accessible surface area has so far prevented FGS-based electrodes from exceeding the performance of conventional carbonaceous materials. To maximize energy density, we therefore must engineer FGS-based electrodes with high ion-accessible SSA (i.e., high C_G) which, at the same time, exhibit high ρ_{eff} and therefore high f.

The effective density ρ_{eff} is an inverse measure for the electrode pore volume, i.e., it is directly related to the size distribution and number of pores within an FGS electrode. While a wealth of information exists on the formation of multi-scale porosity during aggregation of spherical particles,[43] very little is known about the structure of aggregated graphene. We envision that both intra-lamellar pores (the primary pores between the sheets) as well as inter-aggregate pores will exist, as depicted in Figure 2a. These inter-aggregate pores are found in almost all consolidated particulate materials (unless they can be grown as single crystals) and arise because of the statistical nature of the particle aggregation process.[43] As a result, the electrode structure is "locked" in a low density state. For FGS-based electrodes, ρ_{eff} could be maximized if the volume of these inter-aggregate pores was minimized and the intra-lamellar pores were just large enough to accommodate the electrolyte ions (assuming ionic transport was not limiting the performance). Such an optimization of the pore size distribution, however, will have an impact on the ionic transport[44] within the device and thus affect power density which needs to be considered as an additional performance criterion.[1] Further complications arise in the case of small pore space when dry porous electrodes are imbibed with the electrolyte during device fabrication. For example, gases held within the pores can become trapped and block the electrolyte from entering, thus reducing the effective electrode surface area.[1] This phenomenon can be amplified if the electrolyte does not wet the solid with a sufficiently small contact angle. Also, a minimum pore-size is necessary to accommodate the electrolyte ions.[2,25] Thus, the pore structure of an EDLC electrode needs to meet a variety of partially conflicting requirements: Ideally, the entire pore space should be electrolyte-accessible, i.e., electrolyte-filled, interconnected, and sufficiently large to not only allow for the accommodation[45] but also the efficient transport of ions. At the same time, the total pore volume needs to be small such that dense packing of the active material is achieved.

To meet these requirements, we have developed a new strategy for fabricating FGS-based EDLC electrodes using ILs as electrolytes. We summarize our approach in Figure 2b: Instead of imbibing the electrolyte into a high SSA dry electrode with a predefined porous structure[1] or performing a solvent exchange as a final processing step,[8] we introduce the IL at an early stage of the electrode fabrication process. Graphene oxide is first dispersed in water (Fig. 2b, (i)) where it forms a charge-stabilized dispersion.[46,47] Addition of a water-soluble IL screens the charge on the graphene oxide, destabilizes the dispersion, and results in the formation of a gel (Fig. 2b, (ii)). After subsequent consolidation by evaporation of the water (Fig. 2b, (iii)), the graphene oxide is partially reduced thermally in order to obtain the final, electrically conducting electrode material (Fig. 2c), eliminating processing steps such as the drying of GO prior to thermal exfoliation[30,31] or the washing steps required to remove reactants after chemical reduction.[32] We demonstrate that IL remains between the sheets during this process, yielding a compacted FGS/IL nanocomposite. The IL acts not only as the electrolyte but also as a "spacer" maintaining high ion-accessible surface area of the graphene oxide during consolidation. Our procedure eliminates the necessity of imbibing IL into the porous material, thus avoiding the associated problems with pore filling and avoids the use of inactive spacers which would add "dead weight". By tuning the initial water/IL ratio, we can vary the amount of IL residing in the pores, allowing us to achieve high effective electrode densities ($f = 40$ wt%) and high capacitance $C_G = 140$ F/g resulting in values of $E = 17.5$ Wh/kg at $U = 3.0$ V. This E value, as shown in Figure 1b, is significantly higher than

Downloaded on 2013-07-31 to IP 128.112.70.3 address. Redistribution subject to ECS license or copyright; see ecsdl.org/site/terms_use

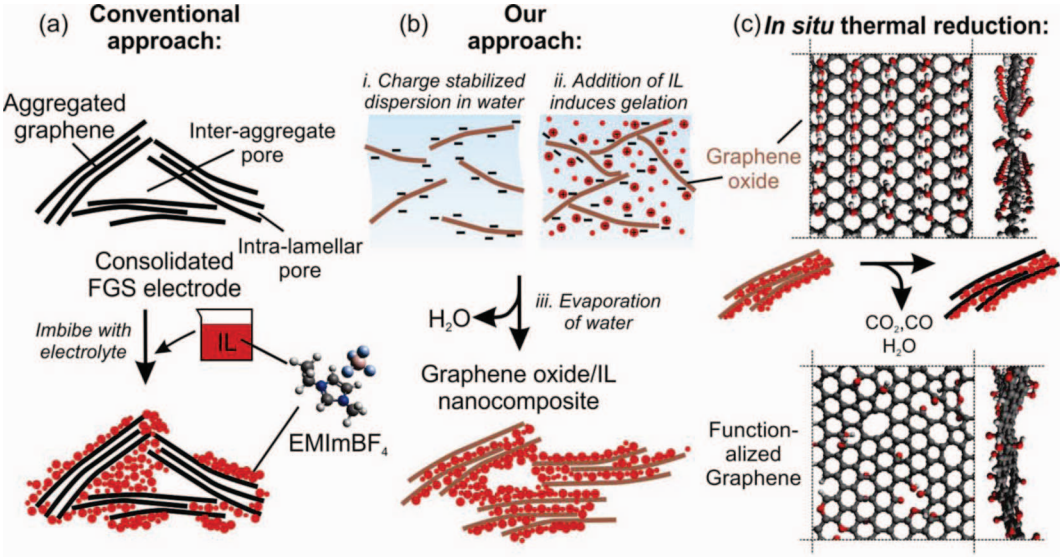

Figure 2. Comparison of conventional electrode fabrication approach with the strategy used in this work. (a) Conventional approach: Consolidation of graphene by evaporative drying or filtration leads to partial restacking of the sheets and a distribution of intra-lamellar and inter-aggregate pores. The IL cannot access all pores either because they are too small, blocked, or the wetting properties are not ideal. (b) Our approach: Dispersion of graphene oxide in water (i) followed by the addition of $EMImBF_4$ (ii). When the water component is removed by evaporation (iii), the $EMImBF_4$ remains between the sheets acting both as the working electrolyte and as a spacer, maintaining a high SSA. (c) In-situ thermal reduction: Schematics of the chemical structures of the involved materials (generated with Avogadro) are shown on the left. The graphene oxide structure is based on the Scholz-Boehm model[33,65] for the sake of simplicity as the true structure of GO is currently debated. The FGS model illustrates the presence of lattice defects and oxygen-containing functional groups in the material.

all the energy densities reported in Table I, providing support for the importance of the processing scheme we introduce in this paper. Furthermore, by variation of f through the IL content, we can tune our electrodes from high energy density to high power density behavior.

Experimental

Materials.— GO was produced according to a modified Hummers method.[48] 3 g of natural flake graphite (Asbury grade 3061) and 18 g of $KMnO_4$ were added under stirring to 360 mL of H_2SO_4 and 40 mL of H_3PO_4. The resulting oxidation reaction was allowed to proceed at 50°C for approximately 16 h. The mixture was cooled to room temperature and subsequently added to approximately 400 g of ice. 6 mL of H_2O_2 was added to the suspension causing the slurry to turn from purple/brown to bright yellow. The suspension was distributed into two 500 mL centrifuge tubes and centrifuged for 15 min at 1800 *g* using an IEC Centra GP8R centrifuge (218A rotor). The supernatant was discarded and the material was re-suspended in water. This washing procedure was then repeated with 250 mL of HCl and again with ethanol three to four times until elemental analysis by energy dispersive X-ray spectroscopy (EDS) showed no change in residual chloride. The IL used, 1-ethyl-3-methylimidazolium tetrafluoroborate ($EMImBF_4$), had a purity of >99% (Sigma-Aldrich). This IL was selected because it is miscible with water and is commonly used as an electrolyte for supercapacitors due to its high ionic conductivity and wide electrochemical stability window.[24]

Electrode fabrication.— Ethanol was used to dilute the concentrated GO slurry (obtained from the washing procedure) to a concentration of approximately 10 mg/mL. The diluted GO/ethanol slurry was then mixed with deionized water at a volume ratio of 3:8. Typically 11 mL of this mixture was horn ultrasonicated at 40% amplitude (Vibracell, Sonics & Materials Inc., CT) for 10 min to break apart loosely aggregated GO particles into single graphene oxide sheets. Under stirring, 1 mL of a solution of $EMImBF_4$ in water was then added to the suspension. 450 μL of the resulting mixture was drop-cast onto 1.5 cm diameter Pt disks (99.9% purity) and allowed to dry at room temperature overnight to eliminate the volatile components (i.e., water and ethanol) while the non-volatile IL was retained in the film. The amount of IL added to the water was varied to generate graphene oxide/IL composites with varying IL content. The composite films were then placed in an ashing furnace (Model 47900, Barnstead-Thermolyne, NH) under a flow of nitrogen and heated to various reduction temperatures between 200 and 350°C at a rate of 20°C/min. After reaching the target temperature, the samples were cooled down to room temperature immediately to prevent significant loss of $EMImBF_4$ as a result of decomposition and evaporation of the IL.[49] The use of a binder was found unnecessary because the films remained coherent after evaporative consolidation and thermal reduction, being held together by both the van der Waals forces between FGSs and the capillary forces. Since binder acts as dead-weight in an electrode, the use of a binder-free electrode increases the projected device energy density further.

Characterization of films.— The mass of the films was determined by weighing the Pt disks both before coating and after the application of the coating and the reduction procedure. An extra electrode was coated and thermally reduced in each batch so that the resulting film could be scraped off and analyzed by thermal gravimetric analysis (TGA) and differential scanning calorimetry (DSC) (449 C Jupiter, Erich Netzsch GmbH & Co., Germany) to determine the fraction of $EMImBF_4$ in each electrode batch. This was done by determining the difference in mass between 500°C (after IL decomposition) and 200°C (prior to decomposition). Additional mass loss due to the further reduction of FGSs during this measurement does not contribute significantly (see Results and Discussion). The mass of FGSs on each electrode was determined by multiplying the total mass of the reduced film by the mass fraction of FGSs determined by TGA. Typically, films contained 0.5–1 mg of active material. The C/O ratio of the FGSs before and after reduction was estimated using EDS (INCA x-act, Oxford Instruments, UK attached to a VEGA1 scanning electron microscope, Tescan USA). Our EDS procedure was found capable of determining the correct stoichiometry of the pure IL and closely reproduced the C/O ratio data obtained previously by combustion analysis for FGSs produced by the thermal reduction method.[30,31] Powder X-ray diffraction (XRD) was carried out using a Miniflex II (Rigaku Americas, PA, Cu K_α radiation). The lowest detectable angle of $2\theta = 5^\circ$ corresponds to an upper limit in the observable d-spacing

Downloaded on 2013-07-31 to IP 128.112.70.3 address. Redistribution subject to ECS license or copyright; see ecsdl.org/site/terms_use

of 17.6 Å. The specific surface area of dried films was determined through N_2 adsorption using a Gemini V unit (Micromeritics Instruments) and fitting the isotherm to the Brunauer, Emmett, and Teller (BET)[50] equation.

Electrochemical testing of the electrodes was carried out in a two-electrode configuration using a spring-loaded stainless steel test cell (MTI Corp. CA) and a Celgard 3501 membrane separator pre-soaked with $EMImBF_4$. Electrodes were assembled in an argon-filled glove box (Innovative Technology, MA). A drop of $EMImBF_4$ (10 μL) was placed between each electrode and the membrane before sandwiching them inside the test cell. This drop was added to ensure good ionic contact between the separator and the electrodes and also to show that the C_G of the composite electrodes containing smaller amounts of IL was not limited by an insufficiently small amount of electrolyte. Addition of IL was unnecessary for films with higher IL content. Tests carried out with no additional IL showed no significant difference in performance and therefore the mass of this additional IL was neglected in our estimation of *f*. Cyclic voltammetry, electrochemical impedance spectroscopy (EIS), and galvanostatic charge/discharge tests were carried out on assembled test cells using a computer-controlled potentiostat (VSP, Bio-Logic USA). C_G was calculated using the following equation:

$$C_G = 2\frac{i_{avg}}{\upsilon \cdot m}. \quad [3]$$

When analyzing cyclic voltammograms (CVs), i_{avg} is taken as the average of the absolute anodic and cathodic currents at the midpoint of the CV, υ is the scan rate, and m is the mass of FGSs on one electrode. C_G was also estimated from galvanostatic discharge curves using the same equation with $\upsilon = (U\text{-}U_{drop})/\Delta t$, where $U = 3$ V is the initial potential, U_{drop} is the voltage drop at the reversal of the scan direction due to Ohmic losses and Δt is the time needed to discharge the cell from 3 to 0 V at the discharging current i_{avg}. The equivalent series resistance was calculated as $R_S = U_{drop}/i_{avg}$.

Results and Discussion

Electrode consolidation.— Dispersions of graphene oxide in the water/ethanol mixture are stable, i.e., they show no sign of aggregation or sedimentation over several weeks. This is expected due to the high number density of carboxylic acids, phenolic hydroxyls, and other functional groups present on graphene oxide which dissociate in water and charge-stabilize the suspended sheets.[46,47] Adding $EMImBF_4$, however, causes a significant increase in suspension viscosity, indicating the formation of a graphene oxide/water gel network. Since $EMImBF_4$ is fully miscible with water, and since a similar gelation phenomenon is observed when adding other salts such as NaCl to the system instead of IL, we ascribe this behavior to screening of the charge on the graphene oxide ("salting out") as a result of the ionic strength increase, leading to subsequent partial aggregation of the graphene oxide by attractive van der Waals forces.[51] Drying these gels results in graphene oxide/IL composite films of typically 5–10 μm in thickness which exhibit different degrees of restacking and aggregation depending on $EMImBF_4$ concentration in the initial gel. In Figure 3, we show the XRD data obtained on composite films assembled with varying amounts of $EMImBF_4$. The XRD profiles show that the characteristic spacing between the graphene oxide sheets varies with the amount of IL. In the absence of $EMImBF_4$, we observe an XRD peak at $2\theta \approx 9.1^\circ$ which indicates that restacking to a graphite oxide like structure has occurred and domains with a d_{0002} spacing of 9.7 Å have formed during drying. This spacing is similar to what has been reported in the literature for GO prepared using the same oxidation method employed here (9.5 Å).[48] The restacking of single sheets of graphene oxide into GO is also in accordance with previous studies where suspensions of graphene oxide were dried or filtered.[52] We find that this restacking results in SSAs of less than 10 m^2/g. With increasing $EMImBF_4$ concentration, the XRD peak broadens, decreases in amplitude, and shifts to larger d-spacing (smaller scattering angle, Fig. 3) indicating that $EMImBF_4$ has disrupted the formation of GO domains as evidenced by the increased average distance between the sheets, consistent with the schematic in Figure 2b. Eventually, above 60 wt% $EMImBF_4$, the films become X-ray amorphous. Hence, above 60 wt%, the IL-filled spaces between the graphene oxide sheets (intra-lamellar pores) become too large or too disordered to cause a significant signal in XRD. As discussed above, in addition to IL contained in the intra-lamellar space, IL is also likely present within larger inter-aggregate voids (Fig. 2). Those might be generated at locations where the compressive strength of the graphene oxide gel network exceeds the compressive forces generated by capillary effects as the solvent is removed by evaporation.[53,54] At 60 wt% IL in the composite, ρ_{eff} should be ~0.66 g/cm^3 if the composite were fully dense. However, the measured ρ_{eff} was ~0.46 g/cm^3 indicating the presence of gas-filled inter-aggregate voids within the composite.

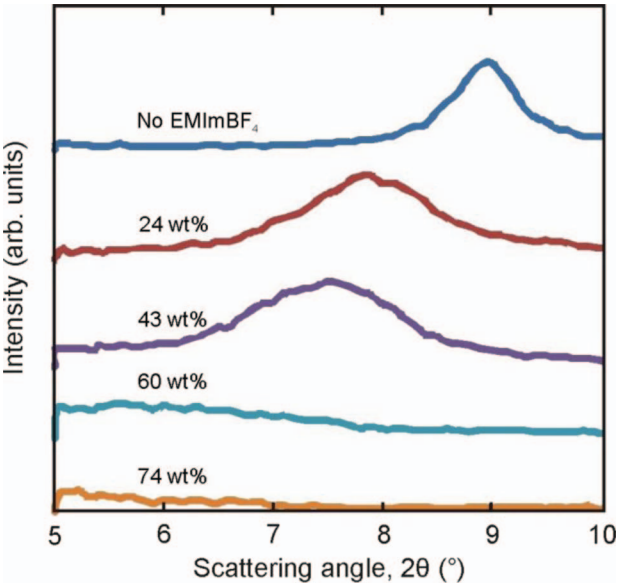

Figure 3. XRD profiles for graphene oxide/$EMImBF_4$ composite films.

To obtain an order of magnitude estimate for the amount of $EMImBF_4$ required to cover the theoretical surface area of graphene oxide (assuming no inter-aggregate voids filled with IL are present), we use the molecular dimensions of the imidazolium cation (0.78 nm × 0.58 nm × 0.33 nm)[55] to estimate the amount of IL necessary for monolayer coverage. The exact orientation of the cation on the surface of graphene oxide is unknown. Assuming that the IL molecule lies flat on graphene oxide (which is the least favorable orientation for achieving high charge density) we approximate that about 70 wt% $EMImBF_4$ is required for a dense packing of IL on both sides of a graphene oxide sheet. This results in two monolayers of IL separating each graphene oxide sheet from the other, i.e., a shared bilayer with an approximate thickness of 2.1–2.4 nm. Theoretically, a shared monolayer is thus expected to form at half of this IL concentration (~35 wt%). The fact that in the range of 35 to 70 wt% of IL we only observe a broad peak shifting to larger d-spacings and no peak corresponding to shared monolayer coverage (shared bilayer spacing lies outside the limits of our XRD unit) suggests that we do not obtain a uniform coverage and an alignment of graphene oxide sheets, in contrast to graphite and GO intercalation compounds which form well-ordered crystalline structures.[56] Instead, the $EMImBF_4$ is randomly distributed, giving rise to an X-ray amorphous structure. Obtaining a uniform IL coating would require that the $EMImBF_4$ completely wet the graphene oxide (vanishing contact angle).[57] The contact angle of $EMImBF_4$ on graphene oxide is unknown, but the fact that we observe neither a distinct peak in XRD nor a phase separation of IL and graphene oxide suggests that $EMImBF_4$ may only be partially wetting. As a consequence, the fraction of the graphene oxide sur-

Downloaded on 2013-07-31 to IP 128.112.70.3 address. Redistribution subject to ECS license or copyright; see ecsdl.org/site/terms_use

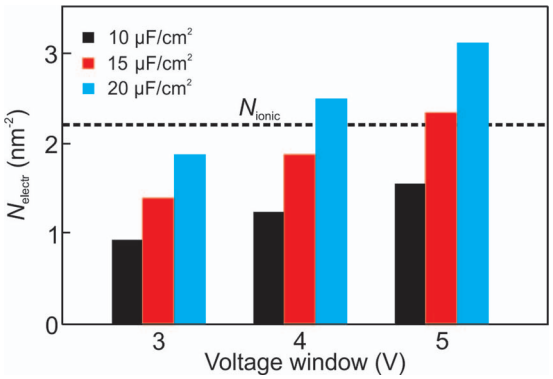

Figure 4. The electronic charge accumulated by an EDLC electrode. $N_{electr} = C_{DL}\ U/2$ assuming a symmetric electrode where each electrode traverses half the potential window.

face area which is in direct contact with $EMImBF_4$ may have been reduced, and voids filled with either IL or air/argon may have formed within the films lowering their ρ_{eff}. Enhancing wettability thus could lead to more uniform coverage and better packing efficiency. Since currently we have no well-ordered reference system to compare to, we cannot determine whether such random arrangement is in fact beneficial for EDLC operation, or whether a more uniform coating and thus maximized accessible surface area will result in the best electrode performance. In the following, we show that packing density can have a direct impact on the electrochemical performance of the IL film (i.e., on the ionic part of the electrochemical double layer) which needs to be taken into account when estimating the minimum amount of IL required for electrode assembly.

We use our estimate of IL packing density on graphene oxide to illustrate how much IL is necessary to charge the electrochemical double layer at high U. To this end, we calculate the electric charge stored for a given value of C_{DL} and U and estimate the number of accumulated electronic charges per nm^2 of electrode material (N_{electr}). This is compared to the corresponding charge density (N_{ionic}) in a monolayer of (monovalent) IL cations which we estimate to be $N_{ionic} \approx 2.2\ nm^{-2}$. In Figure 4, we show several values of N_{electr} for realistic combinations of C_{DL} and different potential windows in comparison to N_{ionic}. The amount of energy stored is limited by the smaller of the two values, and the Figure indicates that with high values of C_{DL} and large voltage windows, N_{electr} is similar to or even greater than N_{ionic}. Therefore, based on our estimations, at least an IL content resulting in coverage in the range from a monolayer to a shared bilayer is required to balance the electronic charge density in an EDLC operating at high voltage. The assumption of a layer of cations without the presence of any counter ions is probably not completely realistic and N_{ionic} might in fact be smaller than estimated. Thus, although reducing the thickness of the IL between each pair of graphene oxide sheets down to a shared monolayer would increase ρ_{eff}, it would also limit the maximum amount of charge that can be stored at the interface. Furthermore, it would certainly limit the rate of charge transport in and out of the pore space between the sheets.

Thermal reduction of graphene oxide/IL composites.— For the electrodes to be used in an EDLC device, the graphene oxide needs to be reduced such that it becomes electrically conducting. Using TGA/DSC, we therefore determined the thermal stability of GO and neat $EMImBF_4$ and identified suitable temperature ranges for reducing the electrode thermally. In Figure 5a, we show TGA/DSC data for the separate thermal decomposition of GO and IL. With GO, around 200°C, mass is lost in an exothermic process, indicative of thermal decomposition and reduction of GO (or graphene oxide).[30,31] The mass of $EMImBF_4$ remains approximately constant until a temperature of 300°C at which mass loss becomes clearly noticeable. Around 500°C, $EMImBF_4$ is completely decomposed in an endothermic process. The characterization of FGS_2/IL composites is shown in Figure 5b. Near 100°C we observe an endothermic mass loss associated with the removal of residual water from the films. The following exothermic mass loss between 200 and 300°C is attributed to the reduction of graphene oxide to FGSs,[30,31] and the final endothermic mass loss at higher temperatures, between 350 and 500°C, is caused by the decomposition of $EMImBF_4$. The final mass obtained is taken to be the mass of the reduced FGSs. In comparison to the TGA data of the neat materials, the GO reduction peak is broadened and shifted to higher temperatures. The mass loss and the endothermic peak corresponding to $EMImBF_4$ decomposition are observed at lower temperatures, shifting from approximately 500 to 350°C as the amount of graphene oxide in the film was increased from 0 to about 70 wt%. Although many studies claim that ILs such as $EMImBF_4$ are stable at temperatures above 400°C, it is now recognized that this apparent stability may be due to heat transfer limitations during fast heating ramps of 10 to 20°C/min.[58] The high thermal conductivity of FGSs[59] as well as their high absorbance[60] compared to the neat IL likely increase the rate of diffusive and radiative heat transfer to the $EMImBF_4$, thus lowering the apparent decomposition temperature. Also, we cannot rule out the possibility that FGSs may catalyze the decomposition of the IL. The difference in temperature between thermal reduction of graphene oxide and $EMImBF_4$ decomposition results in the existence of a temperature window within which graphene oxide can be thermally reduced without significantly decomposing the

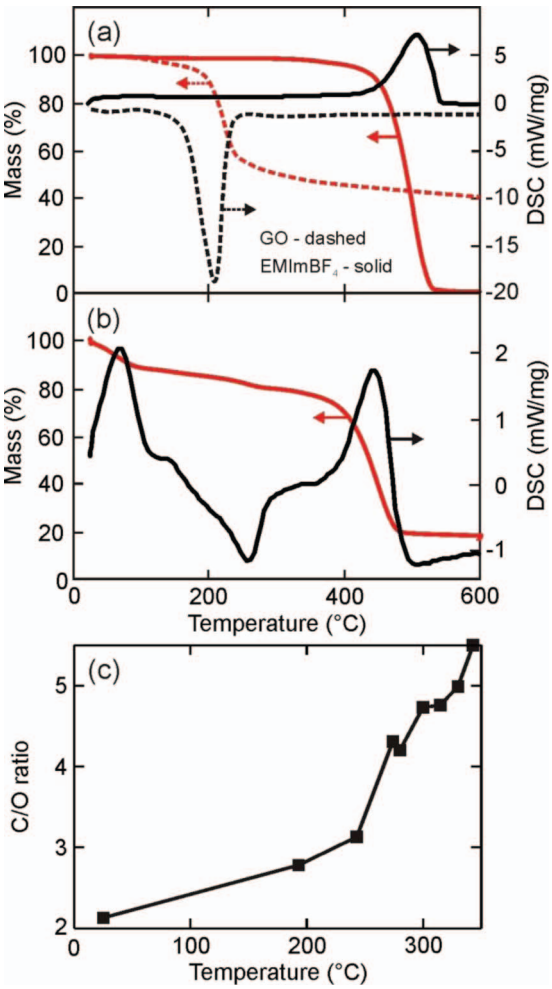

Figure 5. (a) TGA/DSC of neat GO and $EMImBF_4$. (b) TGA/DSC of an electrode composite (FGS_2/$EMImBF_4$) prior to thermal reduction. (c) C/O ratio of thermally reduced FGSs estimated by EDS as a function of composite heat-treatment temperature.

Downloaded on 2013-07-31 to IP 128.112.70.3 address. Redistribution subject to ECS license or copyright; see ecsdl.org/site/terms_use

$EMImBF_4$. We note that a fraction of the mass loss (approximately 5 wt%) in the range between 300 and 500°C is likely caused by further reduction of the FGSs, as suggested by the TGA results for GO reduction alone shown in Figure 5a.

The heat-treatment of composite films results in a drastic color change from an amber-yellow to black at reduction temperatures above 250°C. This increase in absorbance of the films is the consequence of increased electrical conductivity of the initially insulating material due to the increasing number of conjugated and aromatic carbon structures formed during thermal reduction.[60] The C/O ratio of the FGSs as determined by EDS ranges from 2 for the untreated material containing graphene oxide to just above 5 for heat treatments up to 340°C as shown in Figure 5c. The analysis also indicates that the N/F ratio deviated from the expected stoichiometric value of 4:1 for $EMImBF_4$ when temperatures above 270°C were reached (not shown). This deviation implies that IL decomposition begins above 270°C. The slight degree of decomposition was also reflected in the mass loss of the samples during heat-treatment and is consistent with the $EMImBF_4$ content measured by TGA.

Electrochemical characterization.— CVs for an electrode with 78 wt% $EMImBF_4$ are shown in Figure 6a for a series of scan rates between 10 and 100 mV/s. The CVs are all approximately rectangular in shape and display a similar C_G, suggesting that capacitive charging is strictly non-faradaic, as expected for electrodes operated in an aprotic electrolyte. In Figure 6b, the C_G values estimated at 5 mV/s by cyclic voltammetry and at 0.2 A/g by galvanostatic discharge are shown for different IL contents. Values <10 F/g are obtained for films cast in the absence of $EMImBF_4$. C_G increases with increasing $EMImBF_4$ content until above 60 wt%, where C_G reaches saturation at an average value of 136 ± 10 F/g. The relatively constant value of C_G above 60 wt% indicates that the retained ion-accessible SSA does not increase further as more $EMImBF_4$ is added. This suggests that above 60 wt% additional IL, instead of distributing over more FGS surface area and keeping more sheets apart, either increases the average thickness of the IL-filled regions (i.e., intra-lamellar pores and inter-aggregate pores) between the sheets or continues to fill inter-aggregate pores that are only partially filled with IL. The increase in effective pore size with increased IL loading corresponds to our XRD data showing increasing d-spacing.

When we compare electrodes containing varying levels of $EMImBF_4$ above 60 wt% which are all thermally reduced at 270°C, we find a significant difference in the scan rate-dependence of C_G. Figure 6c demonstrates that composite electrodes which contain more $EMImBF_4$ better retain their capacitance at high scan rates. At the highest IL content investigated (80 wt%), C_G decreases by only 15% when increasing the scan rate from 5 to 100 mV/s. The same trend as that shown in Figure 6c is also observed in galvanostatic discharge testing at various current densities. As shown in Figure 7a, the corresponding R_S decreases from 100 to 30 Ω when the IL content is varied between 45 and 80 wt%. These results suggest that by varying the IL content we change the ionic conductivity of the FGS/IL composite network by increasing the size and number of ionic paths. This corresponds well to the hypothesized increase in the size of intra-lamellar pores filled with $EMImBF_4$ as the IL content is increased. It is also likely that the amount of IL in the inter-aggregate voids increases, which is expected to improve the ionic conductivity even further. Since we do not observe a decrease in rate performance or increase in R_S with increasing IL content, at least for the IL contents studied, the electrical contact between the graphene sheets is not severely affected by the increased IL loading. Should a loss of electrical conductivity have occurred, it is over-compensated by the simultaneous improvement in ionic transport. This view is also supported by the absence of a significant increase in C_G at higher loadings, as would be expected if FGS-FGS contact area were lost and more surface area were ion-accessible. As discussed above, the graphene oxide aggregates and yields a gel structure upon addition of $EMImBF_4$ to the suspension, which suggests that the FGSs may form regions of physical and, consequently, electrical contact prior to densification, and the IL cannot separate the sheets at these points during solvent evaporation and further processing.

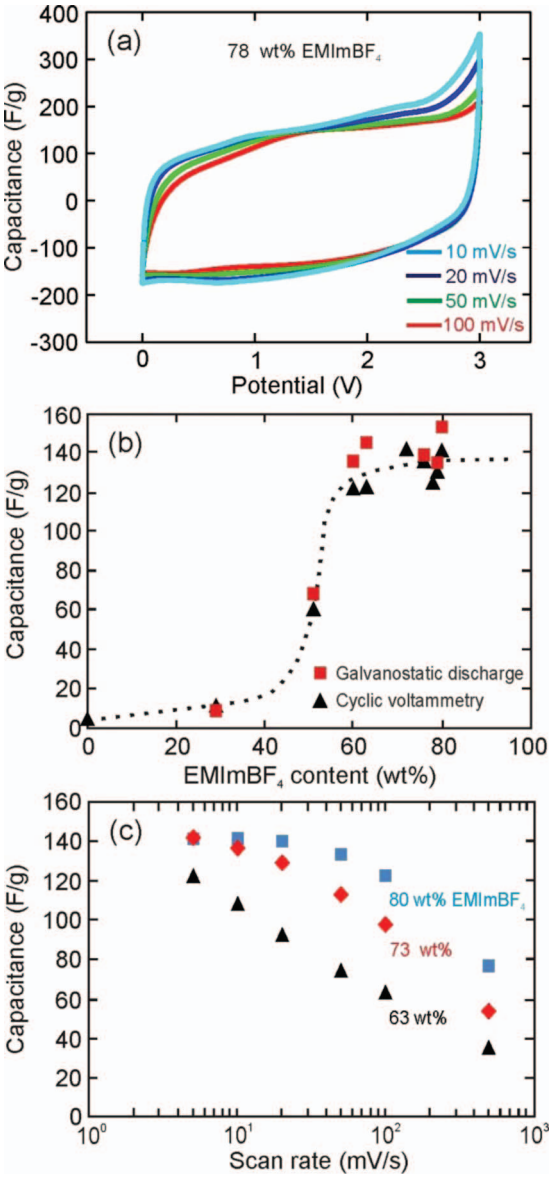

Figure 6. Electrochemical characterization of films heat treated at 270°C. (a) CVs carried out at various scan rates for composite electrodes containing 78 wt% $EMImBF_4$. (b) Capacitance of composite films assembled with varying amounts of $EMImBF_4$ estimated by cyclic voltammetry (scan rate 5 mV/s) and galvanostatic discharge (at 0.2 A/g) in a 3 V potential window. (c) Scan rate dependence of the capacitance for varying $EMImBF_4$ content.

To determine how the degree of reduction affects the performance of the electrodes, we reduced several electrodes containing 75 wt% $EMImBF_4$ (prior to heat-treatment) at various temperatures. When reduced below 250°C, we obtain low C_G (~5 F/g) due to a lack of electronic conductivity. When test cells containing these poorly reduced FGSs are disassembled, the cathode is found to be darker in color than the anode, indicating that it has been electrochemically reduced further during testing. The anode can be brought to a similar state by reversing the polarity of the device and employing it as the cathode in a subsequent measurement; but, by doing so, C_G increases to only ~10 F/g. Thus, the further electrochemical reduction in $EMImBF_4$ is not sufficient to achieve the necessary level of electric conductivity.

Downloaded on 2013-07-31 to IP 128.112.70.3 address. Redistribution subject to ECS license or copyright; see ecsdl.org/site/terms_use

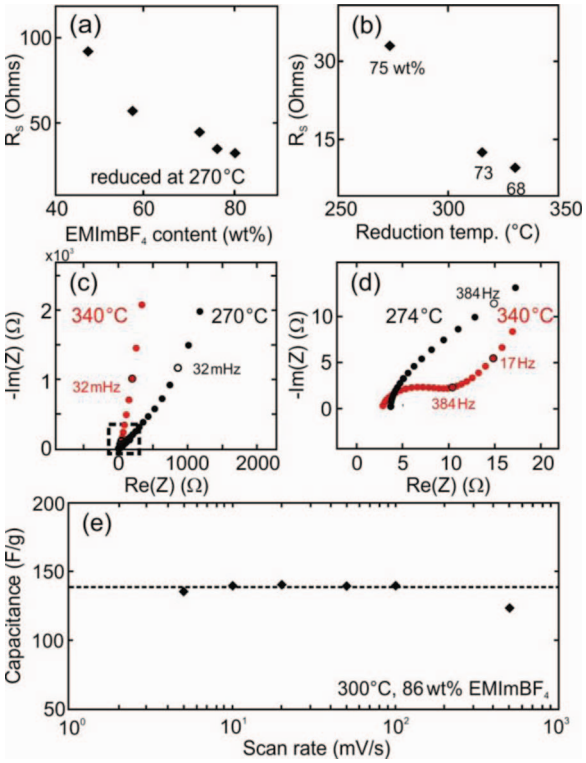

Figure 7. Effect of temperature and IL content on the electrode resistance. (a) R_S estimated from the voltage drop in galvanostatic discharge carried out at 3 V for films assembled with varying amounts of $EMImBF_4$. (b) R_S estimated from the voltage drop in galvanostatic discharge after charging to 3 V for films treated at various reduction temperatures. The initial IL content in all films was 75 wt% and the final IL content is indicated under the data points. (c) EIS measurements at a DC bias of 0 V for electrodes heat treated at two different temperatures. (d) Magnified view of the high frequency region of the Nyquist plot shown in (c). (e) Scan rate dependence of the capacitance of an electrode with 86 wt% $EMImBF_4$ heat treated at 300°C.

Electrodes reduced at different temperatures above 250°C show only small variations in C_G at a low scan rate of 5 mV/s. With increased scan rate, however, differences between electrodes treated at different temperatures became apparent, indicating that, besides ionic transport, electrode conductivity is a performance-limiting factor in our system as well. We therefore examined the effect of heat-treatment on R_S of electrodes with the same initial content of 75 wt% $EMImBF_4$ (Fig. 7a). R_S drops from 33 to 10 Ω as the reduction temperature is increased from 270 to 340°C (Fig. 7b). As indicated in Figure 7b, the decrease in R_S with increasing reduction temperature is accompanied by a loss of IL from the films. Since the loss of IL does not increase the resistance suggests that, in this case, our system is mainly limited by electronic transport. The change in electrode resistance is also apparent in the Nyquist plots of impedance spectra shown in Figure 7c, 7d. Films reduced at 270°C exhibit a Warburg-like constant phase impedance in the mid frequency range, typically associated with ion migration limitations in porous electrodes.[44] Warburg-like behavior is strongly reduced and consequently the diffusion limitations are lessened in electrodes reduced at 340°C. However, as mentioned above, the high-temperature heat-treatment is accompanied by a significant loss of IL. This should have extended the constant phase behavior to lower frequencies (increased diffusive limitation) compared to the result obtained with lower reduction temperature. Since the opposite is observed, in our case the Warburg-like behavior is probably predominantly effected by electronic transport effects within the FGS network which, at this low degree of thermal reduction and comparably high IL content, may dominate over ionic diffusion effects. A similar phenomenon has been observed in impedance spectra measured for semiconductors such as TiO_2 used in dye-sensitized solar cells,[61] and at the lowest C/O ratios tested, our reduced graphene oxide may exhibit semiconducting behavior[62,63] further supporting our conjecture that Warburg-like behavior at low reduction temperatures is an electronic effect. In future work, we hope to determine a method which we can use to independently assess the electronic and ionic resistances in our system to better clarify this behavior.

When high reduction temperatures are applied to the electrodes with the largest IL content, it is possible to achieve nearly constant C_G over a wide range of scan rates. As shown in Figure 7e, films thermally treated at 300°C and containing 86 wt% $EMImBF_4$ retained more than 90% of their capacitance (143 F/g) at scan rates up to 500 mV/s. This value of C_G is one of the highest reported at such a high rate for electrodes using an IL as the electrolyte. For example, in a recent study[64] carried out with electrodes of similar thickness (7–30 μm) it has been demonstrated that activated graphene retains only 72% of the electrode's capacitance (120 F/g) at 400 mV/s despite the use of a higher-conductivity organic electrolyte. Adjusting the scan rate dependence and R_S by tuning the IL content could thus provide a convenient means for preparing electrodes for special high power applications. We would expect the rate capability to keep increasing with improvements to both the thermal reduction protocol and the amount of IL. However, at some point the electronic conductivity will likely suffer due to decreased FGS-FGS contact area. We did not explore combinations of higher temperature treatments and higher IL contents than 86 wt%. At higher IL loadings we expect to reach the point where the composite is no longer a coherent film but a slurry which may no longer be processed into an electrode. As estimated in Table I, binder-free graphene-based electrodes with IL content larger than 93 wt% have been fabricated by Yang et al.[8] and thus we expect films to remain coherent, at least, up to this IL content.

To properly compare our results to other FGS/IL data reported in the literature, we must consider the mass of both the FGSs and the IL as explained in the introduction. Our approach provides direct control over the fraction of each component in the electrodes, and in the thick electrode limit we only need to subtract the IL content from 100% to obtain the weight fraction *f*. Already at relatively low IL content of 60 wt% ($f = 40$ wt%) we achieve values of C_G up to 140 F/g, and, therefore, according to Eq. 1 reach energy densities up to $E = 17.5$ Wh/kg at only 3 V operating voltage. Compared to values of E from the literature (Table I) which range from 5 to 13.8 Wh/kg for FGS-based electrodes and which have been obtained with $U > 3$ V, our approach thus yields significantly increased energy density. Preliminary tests have shown that we can operate our electrodes at $U = 3.5$ V, which for our best electrodes increases E to about 24 Wh/kg. We have achieved these values with thin film electrodes, similar to the other studies discussed in Table I.[6–8] We therefore need to investigate whether the improved performance obtained with our consolidation approach can be maintained as we develop our process further and increase electrode thickness.

From our data we can also estimate the volumetric capacitance C_V (in F/cm^3) and ρ_{eff}, for the 60 wt% IL case using their pure component densities (IL: $\rho_I = 1.3$ g/cm^3, FGSs: $\rho_a = 2.2$ g/cm^3). If we assume the absence of gas-filled voids in the material we obtain $C_V \approx 93$ F/cm^3 and $\rho_{eff} \approx 0.66$ g/cm^3. However, since this estimate represents an upper limit for C_V, we also determined the volume of our electrodes by measuring their approximate thickness and diameter. These measurements indicate that we achieve only approximately 70% of the theoretically estimated bulk density (~0.46 g/cm^3), leading to an estimated C_V of 65 F/cm^3 which is still the highest reported for an FGS-based electrode in an IL.

Conclusions

We have demonstrated a new strategy for the preparation of high-performance graphene-based electrodes for EDLCs with IL electrolytes. Instead of using a porous electrode structure and imbibing the electrolyte or applying solvent exchange techniques, we employ an approach which results in the IL acting both as electrolyte and

Downloaded on 2013-07-31 to IP 128.112.70.3 address. Redistribution subject to ECS license or copyright; see ecsdl.org/site/terms_use

spacer between functionalized graphene improving the ion-accessible surface area. Composites assembled with increasing amounts of IL increase the ion-accessible surface area of the electrodes and improve the performance of the EDLC electrodes at high scan rates by effecting changes in the pore structure of the electrode composite. The mass-specific capacitance of the electrodes reaches values as high as 140 F/g at an effective electrode density of $\rho_{eff} \approx 0.46$ g/cm^3 (60 wt% IL) resulting in a high energy density (17.5 Wh/kg at 3 V) and volumetric capacitance (65 F/cm^3). At a higher IL content of 80 wt%, i.e., at lower electrode density, the electrodes retain over 90% of their maximum capacitance at scan rates up to 500 mV/s. This constitutes the best capacitance retention at high rates reported for thin film carbonaceous electrodes operated in an IL.

Several steps in this approach need to be further improved before our results can be extended to predict the performance of a packaged device. Our current drop-casting approach yields thin film electrodes, and it is known that in many cases electrode performance decreases with increasing thickness.[2] Furthermore, the rate capabilities improve significantly with increasing IL content but this increase negatively affects C_V. Although our approach is promising, we believe there is room for improvement which will be facilitated by a deeper understanding of the interactions between various types of FGSs and ILs and their aggregation behavior to both improve the ion-accessible SSA while maximizing ionic transport within the composite matrix. Electronic transport could be improved by developing better reduction strategies which increase the C/O ratio without decomposing the IL, or, alternatively, by extending our electrode assembly approach to FGSs that have been thermally or chemically reduced to a higher C/O ratio prior to dispersion and assembly.

Acknowledgments

This work was supported by the Pacific Northwest National Laboratory under grant number DE-AC05-76RL01830, the Princeton University Intellectual Property Development Fund, and an Army Research Office (ARO)/Multidisciplinary Research Initiative (MURI) under grant number W911NF-09-1-0476. S. K. and C. P. acknowledge support from a DOD SBIR under contract number W9111QX-11-C-0079.

References

1. B. E. Conway, *Electrochemical Supercapacitors: Scientific Fundamentals and Technological Applications*. Kluwer Academic: New York, (1999).
2. Y. Gogotsi and P. Simon, *Science*, **334**, 917 (2011).
3. Y. Zhu, S. Murali, M. D. Stoller, K. J. Ganesh, W. Cai, P. J. Ferreira, A. Pirkle, R. M. Wallace, K. A. Cychosz, M. Thommes, D. Su, E. A. Stach, and R. S. Ruoff, *Science*, **332**, 1537 (2011).
4. A. G. Pandolfo and A. F. Hollenkamp, *J. Power Sources*, **157**, 11 (2006).
5. C. Liu, Z. Yu, D. Neff, A. Zhamu, and B. Z. Jang, *Nano Lett.*, **10**, 4863 (2010).
6. M. F. El-Kady, V. Strong, S. Dubin, and R. B. Kaner, *Science*, **335**, 1326 (2012).
7. T. Y. Kim, H. W. Lee, M. Stoller, D. R. Dreyer, C. W. Bielawski, R. S. Ruoff, and K. S. Suh, *ACN Nano*, **5**, 436 (2010).
8. X. Yang, J. Zhu, L. Qiu, and D. Li, *Adv. Mater.*, **23**, 2833 (2011).
9. D. Bélanger, L. Brousse, and J. W. Long, *Interface*, **17**, 49 (2008).
10. M. Inagaki, H. Konno, and O. Tanaike, *J. Power Sources*, **195**, 7880 (2010).
11. Y. Y. Shao, J. Wang, M. Engelhard, C. M. Wang, and Y. H. Lin, *J. Mater. Chem.*, **20**, 743 (2010).
12. S. R. C. Vivekchand, C. S. Rout, K. S. Subrahmanyam, A. Govindaraj, and C. N. R. Rao, *J. Chem. Sci.*, **120**, 9 (2008).
13. M. D. Stoller, S. J. Park, Y. W. Zhu, J. H. An, and R. S. Ruoff, *Nano Lett.*, **8**, 3498 (2008).
14. W. Lv, D.-M. Tang, Y.-B. He, C.-H. You, Z.-Q. Shi, X.-C. Chen, C.-M. Chen, P.-X. Hou, C. Liu, and Q.-H. Yang, *Acs Nano*, **3**, 3730 (2009).
15. J. Yan, T. Wei, B. Shao, F. Ma, Z. Fan, M. Zhang, C. Zheng, Y. Shang, W. Qian, and F. Wei, *Carbon*, **48**, 1731 (2010).
16. Y. Chen, X. Zhang, P. Yu, and Y. W. Ma, *J. Power Sources*, **195**, 3031 (2010).
17. X. A. Du, P. Guo, H. H. Song, and X. H. Chen, *Electrochim. Acta*, **55**, 4812 (2010).
18. L. T. Le, M. H. Ervin, H. W. Qiu, B. E. Fuchs, and W. Y. Lee, *Electrochem. Commun.*, **13**, 355 (2011).
19. Y. Chen, X. O. Zhang, D. C. Zhang, P. Yu, and Y. W. Ma, *Carbon*, **49**, 573 (2011).
20. K. Zhang, B. T. Ang, L. L. Zhang, X. S. Zhao, and J. Wu, *J. Mater. Chem.*, **21**, 2663 (2011).
21. Y. W. Zhu, S. Murali, M. D. Stoller, A. Velamakanni, R. D. Piner, and R. S. Ruoff, *Carbon*, **48**, 2118 (2010).
22. V. Khomenko, E. Raymundo-Pinero, E. Frackowiak, and F. Beguin, *Appl. Phys. a-Mater*, **82**, 567 (2006).
23. M. Armand, F. Endres, D. R. MacFarlane, H. Ohno, and B. Scrosati, *Nat. Mater.*, **8**, 621 (2009).
24. A. M. O'Mahony, D. S. Silvester, L. Aldous, C. Hardacre, and R. G. Compton, *J. Chem. Eng. Data*, **53**, 2884 (2008).
25. C. Largeot, C. Portet, J. Chmiola, P.-L. Taberna, Y. Gogotsi, and P. Simon, *J. Am. Chem. Soc.*, **130**, 2730 (2008).
26. M. Lazzari, M. Mastragostino, and F. Soavi, *Electrochem. Commun.*, **9**, 1567 (2007).
27. A. Balducci, R. Dugas, P. L. Taberna, P. Simon, D. Plée, M. Mastragostino, and S. Passerini, *J. Power Sources*, **165**, 922 (2007).
28. M. M. Hantel, T. Kaspar, R. Nesper, A. Wokaun, and R. Kötz, *Electrochem. Comm.*, **13**, 90 (2011).
29. Y. Zhu, M. D. Stoller, W. Cai, A. Velamakanni, R. D. Piner, D. Chen, and R. S. Ruoff, *Acs Nano*, **4**, 1227 (2010).
30. H. C. Schniepp, J. L. Li, M. J. McAllister, H. Sai, M. Herrera-Alonso, D. H. Adamson, R. K. Prud'homme, R. Car, D. A. Saville, and I. A. Aksay, *J. Phys. Chem. B*, **110**, 8535 (2006).
31. M. J. McAllister, J. L. Li, D. H. Adamson, H. C. Schniepp, A. A. Abdala, J. Liu, M. Herrera-Alonso, D. L. Milius, R. Car, R. K. Prud'homme, and I. A. Aksay, *Chem. Mater.*, **19**, 4396 (2007).
32. S. Stankovich, D. A. Dikin, R. D. Piner, K. A. Kohlhaas, A. Kleinhammes, Y. Jia, Y. Wu, S. T. Nguyen, and R. S. Ruoff, *Carbon*, **45**, 1558 (2007).
33. K. N. Kudin, B. Ozbas, H. C. Schniepp, R. K. Prud'homme, I. A. Aksay, and R. Car, *Nano Lett.*, **8**, 36 (2008).
34. M. A. Pope, C. Punckt, and I. A. Aksay, *J. Phys. Chem. C*, **115**, 20326 (2011).
35. J. L. Xia, F. Chen, J. H. Li, and N. J. Tao, *Nat. Nanotechnol.*, **4**, 505 (2009).
36. M. D. Stoller, C. W. Magnuson, Y. Zhu, S. Murali, J. W. Suk, R. Piner, and R. S. Ruoff, *Energy Environ. Sci.*, **4**, 4685 (2011).
37. O. Kimizuka, O. Tanaike, J. Yamashita, T. Hiraoka, D. N. Futaba, K. Hata, K. Machida, S. Suematsu, K. Tamamitsu, S. Saeki, Y. Yamada, and H. Hatori, *Carbon*, **46**, 1999 (2008).
38. L. Yan, C. Punckt, I. A. Aksay, W. Mertin, and G. Bacher, *Nano Lett.*, **11**, 3543 (2011).
39. C. Punckt, F. Muckel, S. Wolff, I. A. Aksay, C. A. Chavarin, G. Bacher, and W. Mertin, *Appl. Phys. Lett.*, **102**, (2013).
40. V. Lockett, R. Sedev, J. Ralston, M. Horne, and T. Rodopoulos, *J. Phys. Chem. C*, **112**, 7486 (2008).
41. C. Punckt, M. A. Pope, J. Liu, Y. H. Lin, and I. A. Aksay, *Electroanal*, **22**, 2834 (2010).
42. L. L. Zhang and X. S. Zhao, *Chem. Soc. Rev.*, **38**, 2520 (2009).
43. W. Y. Shih, J. Liu, W. H. Shih, and I. A. Aksay, *J. Stat. Phys.*, **62**, 961 (1991).
44. R. de Levie, *Electrochim. Acta*, **8**, 751 (1963).
45. M. Lazzari, F. Soavi, and M. Mastragostino, *Fuel Cells*, **10**, 840 (2010).
46. T. Hwa, E. Kokufuta, and T. Tanaka, *Phys. Rev. A*, **44**, R2235 (1991).
47. T. Szabó, O. Berkesi, P. Forgó, K. Josepovits, Y. Sanakis, D. Petridis, and I. Dékány, *Chem. Mater.* **18**, 2740 (2006).
48. D. C. Marcano, D. V. Kosynkin, J. M. Berlin, A. Sinitskii, Z. Sun, A. Slesarev, L. B. Alemany, W. Lu, and J. M. Tour, *Acs Nano*, **4**, 4806 (2010).
49. M. J. Earle, J. M. S. S. Esperanca, M. A. Gilea, J. N. Canongia Lopes, L. P. N. Rebelo, J. W. Magee, K. R. Seddon, and J. A. Widegren, *Nature*, **439**, 831 (2006).
50. S. Brunauer, P. H. Emmett, and E. Teller, *J. Am. Chem. Soc.*, **60**, 309 (1938).
51. W. B. Russel, D. A. Saville, and W. R. Schowalter, *Colloidal dispersions*. Cambridge University Press: Cambridge; New York, (1989).
52. D. A. Dikin, S. Stankovich, E. J. Zimney, R. D. Piner, G. H. B. Dommett, G. Evmenenko, S. T. Nguyen, and R. S. Ruoff, *Nature*, **448**, 457 (2007).
53. G. W. Scherer, *J. Am. Ceram. Soc.*, **73**, 3 (1990).
54. L. Bergstrom, C. H. Schilling, and I. A. Aksay, *J. Am. Ceram. Soc.*, **75**, 3305 (1992).
55. S. Liu, W. Liu, Y. Liu, J.-H. Lin, X. Zhou, M. J. Janik, R. H. Colby, and Q. Zhang, *Polymer Int.*, **59**, 321 (2010).
56. L. B. Ebert, *Annu. Rev. Mater. Sci.*, **6**, 181 (1976).
57. L. Leger and J. F. Joanny, *Rep. Prog. Phys.*, **55**, 431 (1992).
58. D. M. Fox, J. W. Gilman, H. C. De Long, and P. C. Trulove, *J. Chem. Thermodyn.*, **37**, 900 (2005).
59. A. A. Balandin, S. Ghosh, W. Bao, I. Calizo, D. Teweldebrhan, F. Miao, and C. N. Lau, *Nano Lett.*, **8**, 902 (2008).
60. M. Acik, G. Lee, C. Mattevi, M. Chhowalla, K. Cho, and Y. J. Chabal, *Nat. Mater.*, **9**, 840 (2010).
61. J. Bisquert, *J. Phys. Chem. B*, **106**, 325 (2001).
62. S. Wang, R. Wang, X. Wang, D. Zhang, and X. Qiu, *Nanoscale*, **4**, 2651 (2012).
63. X. Wu, M. Sprinkle, X. Li, F. Ming, C. Berger, and W. A. de Heer, *Phys. Rev. Lett.*, **101**, 026801 (2008).
64. L. L. Zhang, X. Zhao, M. D. Stoller, Y. Zhu, H. Ji, S. Murali, Y. Wu, S. Perales, B. Clevenger, and R. S. Ruoff, *Nano Lett.*, **12**, 1806 (2012).
65. V. W. Scholtz and H. P. Boehm, *Z. Anorg. Allg. Chem.*, **369**, 327 (1969).

Downloaded on 2013-07-31 to IP 128.112.70.3 address. Redistribution subject to ECS license or copyright; see ecsdl.org/site/terms_use